

Flow Characterization of a Pulsating Heat Pipe through the Wavelet Analysis of Pressure Signals

Roberta Perna¹, Mauro Abela¹, Mauro Mameli¹, Alessandro Mariotti², Luca Pietrasanta³, Marco Marengo³, Sauro Filippeschi¹

¹ Department of Energy, Systems Land and Construction Engineering. University of Pisa, Largo L. Lazzarino, Pisa, Italy.

² Department of Civil and Industrial Engineering. University of Pisa, Via G, Caruso 8, 56122 Pisa, Italy.

³ Advanced Engineering Centre, School of Computing, Engineering and Mathematics. University of Brighton, Lewes Road, BN2 4GJ Brighton, UK.

Corresponding author e-mail: c.robertaina@gmail.com

Abstract

Pulsating Heat Pipes are two phase passive heat transfer devices characterized by a thermally induced two phase oscillating flow. The correct detection of the dominant frequencies of such oscillations is fundamental to fully characterize the device thermofluidic operation but the studies available in the literature are very heterogenous and results are often discordant. In this work, the concept of dominant frequency in Pulsating Heat Pipes is thoroughly discussed and defined analytically. The wavelet transform is used to characterize the fluid pressure signal in the frequency domain varying the heat power input at the evaporator and in the condenser zone of a full-scale Pulsating Heat Pipe tested in microgravity conditions. During the slug-plug flow regime, the dominant frequencies falls in the range 0.6 – 0.9 Hz, showing an increasing trend with the heat load input. The Cross-Correlation reveals that the two signals at the evaporator and at the condenser are very similar. Finally, the instantaneous angle of phase is calculated and lies between 310 and 360 deg. This value can be physically interpreted as a repeatable time shift between the two signals that can be used to evaluate the flow local mean velocity (0.09 – 0.13 m/s) constituting a valuable alternative to the visualization techniques.

Keywords: Pulsating Heat Pipe, Frequency, Wavelet Cross Correlation, Flow velocity.

Nomenclature			
C_b	bending pressure loss coefficients	g	Gravitational acceleration (m/s^2)
ψ	complex mother function	f	Frequency (Hz)
C_ψ	admissibility condition	T	Temperature ($^{\circ}C$)
$\hat{\psi}(\omega)$	fourier transform	P	Pressure (Pa)
W_x	wavelet transform	N_{wt}	number of samples
a	scale dilation parameter (1/Hz)	N	Number of turns
τ	translation parameter (s)	\dot{Q}	heat load input (W)
P_{W_x}	wavelet power spectrum	c	damping action
W_{xy}	wavelet cross scalogram	m	Mass (Kg)
$WLCC$	wavelet local correlation coefficient	ρ	Density (Kg/m^3)
θ_{x-y}	instantaneous angle of phase (deg)	L	Length (m)
CoW_{xy}	wavelet co-scalogram	μ	dynamic viscosity (Pa s)
Subscripts			
w	wall	e	evaporator
D	dominant	c	condenser

Max	maximum	v	vapour
C	characteristic	l	liquid
Ac	acquisition	f	fluid
An	analysis	e	evaporator

1 Introduction

2 Thermally induced oscillations in two phase confined slug flows largely affect the operation of
 3 heat transfer devices such as micro-channel heat exchangers (MHE) and wickless heat pipes,
 4 also known as Pulsating Heat Pipes (PHPs). Regarding MHEs, these phenomena may lead to
 5 flow instabilities that are often detrimental for the device operation, causing a flow reversal to
 6 the inlet manifold [1] while, in PHPs, they constitute their vary basic working principle [2]. The
 7 frequency analysis of experimental data has been proved to be a promising tool to characterize
 8 such unstable behaviours in particular through the detection of dominant frequencies in the flow
 9 motion. The present work proposes to apply the wavelet transform to the fluid local pressure
 10 signal of a PHP in the evaporator and in the condenser zones, to rigorously define the concept
 11 of dominant and characteristic frequencies and link them to the device physical behaviour.
 12 Frequency analysis on PHP have already been performed in the literature but, as shown in the
 13 following state of the art, results are quite heterogeneous; Table 1 summarises, in chronological
 14 order, the most relevant works available in literature so far. They can be distinguished according
 15 to three main factors: i) the definition given for the dominant frequency of a PHP signal; ii) the
 16 type of time-frequency technique; iii) the type of experimental signal exploited for the analysis.

Table 1. resume of the literature review

Authors name	Year	Geometry		I.D./O.D. [mm]	Working fluid	Signal	Section	Type of analysis	Frequency [Hz]	Vol. F.R. %	Heat input \dot{Q} [W]	
		Cross-section	Turn									
Xu et al. [3]	2005	tubular	3	2/3	FC-72*	T_w	eva	FT	0.09	70	12	
									<i>close to zero; 0.46; 0.9</i>		25.6	
									–		12	
									<i>close to zero; 0.46</i>		25.6	
Khandekar et al. [16]	2009	tubular	1	2/4	ethanol	P_f	eva	FT	0.1 – 3	60	20	
Zhao et al. [14]	2011	tubular	6	1.65-3.18	water	T_w	eva	FT	-	49.2	210 - 240	
							WT	-				
Mameli et al. [4]	2012	tubular	2	2/4	ethanol	P_f	adia	FT	-	-	40 -100	
Peng et al. [9]	2013	tubular	8	4	ammonia	liquid slug velocity		HHT	$C_b = 0$	3.2	20	-
										2.5	30	
										2.4	40	
					2.3					50		
					2.7					60		
					2					70		
acetone	$C_b = 0.2$	1.8	60									
water	$C_b = 0.5$	1										
Mameli et al. [5]	2014	tubular	2	2/4	ethanol	P_f	adia	FT	-	65	40-100	
Fairley et al. [7]	2015	flat	6	1.5	water	T_w	eva	STFT energy spectrum	< 0.2	70	210 - 240	
								HHT energy spectrum	0.2-0.4		210; 230	
									0.1		240	

								HHT spectrum	< 0.2		210 - 240								
Spinato et al. [10]	2015	Flat	1	1	R245fa**	T_w	eva	TST	-	20	8								
									0.7		22								
									-		36								
																		60	6-8
									1.2	14-32									
									-	34									
Monroe et al. [11]	2017	tubular	4	3.25/4.8	water	T_f	eva adia cond	FT	~2	70	60								
									~3		150								
									~4		275								
						T_w			-										
Chi et al. [15]	2018	tubular	15	1/2	ethanol	T_w	eva	FT	0-0.1	6.7 - 40	14								
											20								
											25								
Ishii et al. [8]	2019	Flat	12	-	water	T_f	eva	FT	-	50	74.4								
									<3		118.3								
											172								
											238								
									2		316								
	405																		
Takawale et al. [6]	2019	Tubular	17	1/2	ethanol	P_f	cond	FT	-	60	64-112								

Legend: FT is Fast Fourier Transform. STFT is Short Time Fourier Transform. HHT is Hilbert-Huang Transform. TST is Time Strip Technique. WT is Wavelet Transform. P_f is fluid pressure. T_f is fluid temperature. T_w is wall temperature. C_b is bending pressure loss coefficients. * Perfluorohexane. ** Pentafluoropropane.

1.1 The dominant frequency issue

Only a few authors provided a definition of dominant frequency so far in the literature. Xu et al. [3] are among the first to introduce the time-frequency analysis as a tool for the PHPs thermofluidic investigation and they define the dominant frequency as a peak of energy in the Power Spectrum. Their work exploits the Fourier Transform (FT) analysis on three wall temperatures signals, in the evaporator and the condenser section at different heat loads. At 12 W, the dominant frequency values (0,1 Hz) are much smaller than those obtained for 25,6 W (0,46 – 0.9 Hz). Mameli et al. [4][5] performed the FT analysis on the pressure signal at different heat input levels without recognizing any peak in the power spectra and thus opening the discussion on whether the FT would be the most suitable tool for the frequency detection. Also, in Takawalea et al. [6], the FT is applied on the pressure signals, but the dominant frequencies cannot be found too. Despite the FT analysis has been exploited more extensively with respect to other techniques, it is intrinsically not able to detect the time range where the dominant frequencies occur, so the analysis is often performed on very large amount of data and it often provides noisy outputs where peaks are hardly recognizable. In this vein, Fairley et al. [7] describe the presence of energy peaks in the Power Spectrum as occurrence of intermittent high-energy oscillations in the PHP evaporator temperature signal. In their study, the Short-Time Fourier Transform (STFT) and Hilbert-Huang Transform (HHT) analyses are performed on the wall temperature and at different heat loads. The Hilbert-Huang energy spectrum shows intermittent oscillations at frequencies between 0,2 and 0,4 Hz. In the Hilbert-Huang marginal spectra, the intermittent high-energy peaks fall in the range 0,02-0,2 Hz. The power spectrum of temperature signal tends to decrease when the heat input increases, in accordance with Ishii et al. [8] and Peng et al. [9] but in opposition with Spinato et al. [10] and Monroe et al. [11]. The results of the STFT are like those obtained with HHT, but the HHT's sharper time and frequency resolution makes some features of the energy spectra more evident. Overall, works derive a definition of dominant frequency only from a visual interpretation of graphical results. In Spinato et al. [10], the Time Strip Technique (TST) [10], a novel synchronized thermal and visual investigation technique, is used to assess the thermal and hydrodynamic behaviours in a single loop PHP. The 3D frequency spectra are computed for the local evaporator and condenser wall temperatures, as well as for the time-strip (or interval in the time domain) intensity at the same locations. Dominant frequencies are 0,6 Hz for FR = 20% and 1,2 Hz for FR = 60%. The condenser signal results are almost absent, compared to the result obtained at the evaporator. In the present work, the Wavelet Transform (WT) is chosen because it can overcome the limits of FT and STFT. In this sense, the WT is a powerful tool with a good capacity for time-frequency localizations and multiresolution representations, giving the possibility to “locate” the eventual dominant frequency in time [12][13]. A rigorous and comparable way to define the dominant frequency of a PHP starting from the wavelet analysis of the fluid pressure signal is proposed in section 3.2.

1.2 Choice of the PHP signals

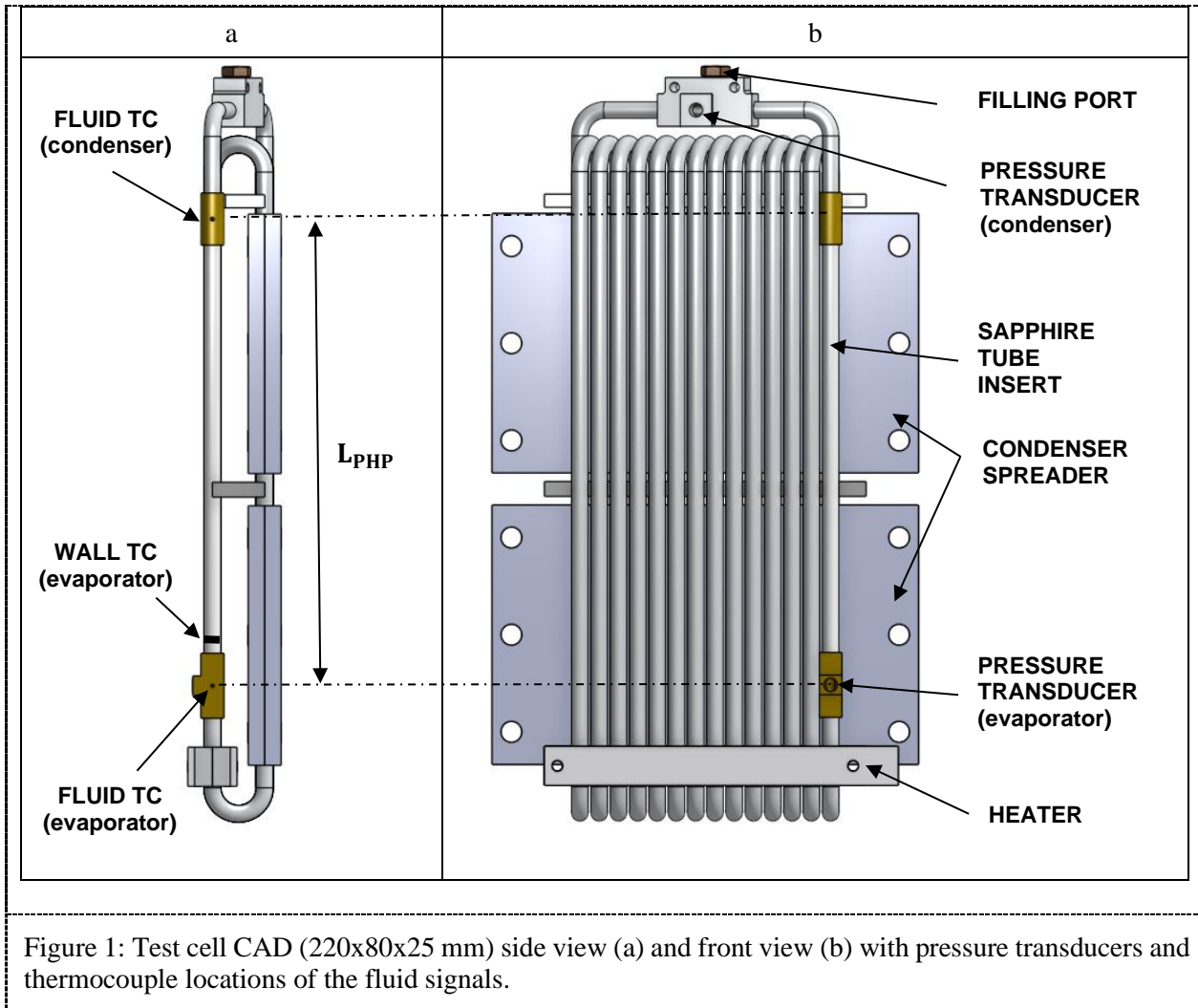
All the techniques mentioned in the previous section are applied to different types of thermo-fluidic signals. Much research analyses the PHP pseudo-steady state, and the most common choice for the signal is the wall temperature. Zhao et al, [14] apply the FT and the WT to the wall temperature signal but no dominant frequency is identified. Chi et al. [15] use the FT on the wall temperature signal too and find frequencies up to 0,1 Hz. Monroe et al. [11] are among the first that compare the results obtained by the wall temperature signal analysis with those obtained by the fluid temperature signal analysis. In their work, two thermocouples (TCs) are placed inside (fluid) and on top (wall) of an operating PHP. The results show that the frequencies of the fluid temperature fall in the range from 2 to 4 Hz, while no frequencies are detected by the wall temperature analysis, due to the thermal inertia of the tube. The FT is also applied by Ishii et al. [8] on the fluid temperature signal. For heat loads of 74,4 to 112 W, there is not any visible peak in the power spectrum, while for 316 W and 415 W the peaks are identified around 2 and 3 Hz. In addition to the signals recorded during the experimental tests, some authors apply the frequency analysis to the numerical output of their models but this may be misleading if the model is not validated, at least partially, against experimental data. Peng et al. [9], for example, present a nonlinear thermomechanical finite-element model of PHP that aims at simulating the slug oscillation, and then calculate the time-varying spatial distributions (HHT) of the slugs velocity by varying different parameters. If the bending pressure loss coefficients C_b and the heat input increase, the frequencies decrease and they fall in the range 1-3,2 Hz. Finally, some authors, apply the Fourier Transform on the fluid pressure signal (e.g. [4], [5]). Among these works Khandekar et al. [16] focus on a steady state and transition state of operation PHP. The frequency falls in the range from 0,1 to 3 Hz. The choice of the fluid pressure signal brings substantial advantages with respect to the others signals (wall and fluid temperatures) because it is directly related to the fluid motion, it is not affected by the probe thermal inertia, thus, it allows to acquire data at a very high sampling rates. As shown in the next sections, the wavelet analysis presented here is performed at first on all the three signals (wall temperature, fluid temperature and fluid pressure) to give proof of the above advantages, then the fluid pressure signal is kept as reference for the whole post processing.

Beyond the standard WT frequency analysis of singular signals, the Cross-Correlation and the calculation of the instantaneous angle of phase between the two signals at the evaporator and at the condenser is also performed to demonstrate that the last can be physically interpreted as a repeatable time shift between the two signals that can be used to evaluate the flow local mean velocity. The flow velocities values obtained by means of the WT analysis are finally compared to those obtained by the InfraRed visualization technique showing a good match and opening a new and valuable alternative for the PHP flow characterization where visualization techniques are not applicable.

2 Experiments and post-processing tools

2.1 Test cell

The PHP test cell consists of an annealed aluminum tube with an inner/outer diameter of 3/5 mm and it is also thoroughly described by Mameli et al. [17]. The tube is folded in a single loop staggered configuration with fourteen turns in the evaporator zone as shown in Figure 1.



An aluminium T-junction (on the top of figure 1 b) allows to close the loop and hosts a miniaturized pressure transducer along with the vacuum and filling port. Two brass connections allow to embed a sapphire tube insert, transparent (transmissivity 0.9) both to the visible and the Medium Wave InfraRed (MWIR), and to host two K-type micro-thermocouples for the fluid temperature measurement, as well as one pressure transducer close to the evaporator section. Two ceramic ohmic heaters supply from a minimum of 18W to a maximum of 180W by means of a programmable power supply, corresponding to an average wall to fluid heat flux from 1,10 to 11,43 W/cm². In particular, the tested heat input levels are $\dot{Q} = 68, 96, 134, 146 \text{ W}$. The backside of the condenser spreaders is cooled down by means of eight Peltier cells and cold plate temperature control system (not shown in figure 1). The main measured variables along with the probes specifications and their maximum errors are shown in table 2. The device is

partially filled with 22 ml of FC-72 (50% vol.). The test rig is then loaded on an Airbus A310 and a total of 93 parabolic trajectories (hypergravity-microgravity-hypergravity) are performed over the three days of flight. The device is oriented in bottom heated mode (the main acceleration field in the flow path direction). During the thermal characterization, the device is heated up at the desired power level before the occurring of the microgravity period, and the power level is kept constant for the whole sequence of parabola. The pressure signals are acquired at 200Hz and the temperature signals as well as the MWIR camera are acquired at 50Hz.

Table 1. Measured quantities and uncertainties.

Parameter	Specs.	Max. error
Tube wall temperature	T-Type thermocouples (0.5mm bead diameter)	± 0.1 °C
Fluid temperature	Omega [®] KMTSS-IM025E-150 K-Type thermocouples (0.25 mm bead diameter)	± 0.2 °C
Fluid Pressure	Keller [®] PAA-M5-HB, 1bar abs	± 500 Pa
Fluid temperature in sapphire section	AIM [®] MWIR camera, (wavelength 3-5 μ m)	± 2 °C
Power Input	GW-Instek [®] . PSH-6006A	± 3 W

2.2 Infrared Analysis

Since the sapphire tube is almost transparent to the radiation in the MWIR spectrum, the images, allowed to measure, not only the temperature distribution of liquid plugs, as already demonstrated in a previous work by the same authors [18], but also their length and velocity. The sapphire tube portion framed by the camera is 65.8 mm long and results in a 701x54 pixel image, therefore the pixel dimension is approximately 93 μ m. Figure 2 shows two consequent time frames of the fluid temperature distribution (orange line) in the mid axis of the transparent extracted from the MWIR images. Note that only when the liquid phase fills completely the channel (liquid slugs), the temperature values are detectable (continuous line). For all the other cases, i.e. vapor bubbles, or dispersed flow, since the vapor phase is almost transparent to the MWIR spectrum, the corresponding temperature is not physically meaningful (dashed line). In any case, the transition regions between higher and lower temperatures correspond to the menisci of a liquid slug. A thorough image analysis is performed by means of a custom Matlab software to detect the liquid slug menisci at each frame and calculate their length and velocity. The liquid slug recognition is performed evaluating the local maxima and minima of the temperature first derivative (black line): a liquid plug is always detected between a maximum and a minimum. Being an adiabatic zone, no evaporation or condensation occurs while the slugs travels through the sapphire tube, thus slugs are expected to maintain the same length throughout all the recorded frames. Indeed, the maximum discrepancy in the length measurement between different frames is 5 pixels and this occurs for less than the 20% of the

frames. The i -th slug velocity over one time step, i.e. between frame $k-1$ and frame k , is defined as

$$v_{i,k} = (x_{i,k} - x_{i,k-1}) f_{ac} \quad (1)$$

where $x_{i,k}$ is the i -th slug center point in frame k , $x_{i,k-1}$ is the i -th slug center point in frame $k-1$ and f_{ac} is the acquisition frequency. It follows that the maximum uncertainty of the instantaneous velocity is $0.093 \cdot 10^{-3} \cdot 5 \cdot f_{ac} \cong 0.023 \text{ m/s}$. The mean velocity is finally evaluated as

$$\bar{v}_{i,IR} = \frac{1}{N_f} \sum_{k=1}^{N_f} v_{i,k} \quad (2)$$

where N_f is the total number of frames. In this case, since the maximum discrepancy in the length measurement between different occurs for less than the 20% of the frames, the maximum uncertainty is tempered as follows $0.2 \cdot 0.093 \cdot 10^{-3} \cdot 5 \cdot f_{ac} \cong 0.004 \text{ m/s}$. The mean velocity values are used in section 3.6 as a reference for the comparison with the mean velocities extracted through the WT analysis.

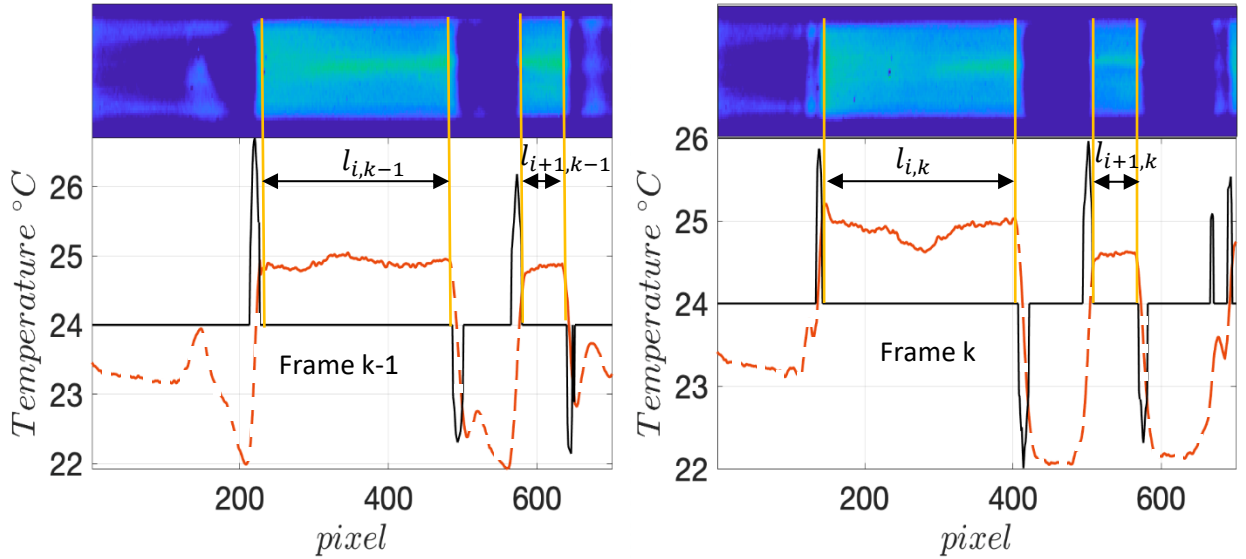


Figure 2: On top, IR images of the sapphire tube. On the bottom, the temperature distribution (orange), the first derivative of temperature distribution (black), plugs ends (yellow).

2.3 Wavelet Transform methodology

The fluctuations of the pressure and temperature signals are characterized through techniques based on the continuous Wavelet Transform (WT). As described by Buresti et al.[12], a wavelet function can be any real or complex function $\psi(t) \in L^2$ that satisfies the following admissibility condition:

$$C_\psi = \int_{-\infty}^{+\infty} |\hat{\psi}(\omega)|^2 |\omega|^{-1} d\omega < \infty \quad (3)$$

where $\hat{\psi}(\omega)$ is the Fourier transform of $|\psi(t)|$. Indeed, to guarantee the reversibility of the transform, C_ψ must be a finite quantity and, in practice, this implies that $\psi(t)$ has zero mean value. Under this admissibility condition, the Wavelet Transform $W_x(a, \tau)$ can be defined as follows:

$$W_x(a, \tau) = \frac{1}{\sqrt{a}} \int_{-\infty}^{+\infty} x(t) \psi^* \left(\frac{t - \tau}{a} \right) dt \quad (4)$$

where $a \in \mathfrak{R}^+$ is the scale dilation parameter and $\tau \in \mathfrak{R}$ is the translation parameter. In the present study, the complex Morlet wavelet $\psi(t) = e^{i\omega_0 t} e^{-t^2/2}$ is used, with a central frequency $\omega_0 = 2\pi$ in order to well-balance time and frequency resolutions (Table 3). For the Morlet wavelet the frequencies f are related to the scales a by $f = \omega_0 / (2\pi a)$, thus in this case, $f = 1/a$. The wavelet power spectrum can be obtained from the integration in time, i.e, for each scale/frequency, the wavelet energy map, as:

$$P_{W_x}(a) = \frac{1}{C_\psi} |W_x(a, \tau)|^2 d\tau \quad (5)$$

In analogy to the signal analysis procedures used in [13], [19], the Wavelet Transform is preferred to STFT for time-frequency analysis because it allows to dynamically increase the frequency resolution at lower frequency values, whereas to increase time resolution at higher frequency values (in STFT the frequency resolution is fixed). Moreover, compared to classical Fourier spectra, the wavelet-based procedure allows to obtain smoother spectra and well defined from the mathematical point of view. The results in the following section are reported in form of time-frequency energy maps $|W_x|^2$, (also called ‘‘scalograms’’) and wavelet spectra P_{W_x} . In the scalogram, the colour represents the energy value at the given time and frequency. The related spectrum will be used for the identification of the dominant frequencies. Given that $W_x(a, \tau)$ and $W_y(a, \tau)$ are, respectively, the complex wavelet transforms of two signals $x(t)$ and $y(t)$, their wavelet cross-scalogram is defined, as:

$$\begin{aligned} W_{x-y}(a, \tau) &= W_x^*(a, \tau) W_y(a, \tau) = \\ &= CoW_{xy}(a, \tau) - i QuadW_{xy}(a, \tau) \end{aligned} \quad (6)$$

It can be shown that the real part of the cross-scalogram, or co-scalogram CoW_{xy} , gives the instantaneous contribution at each frequency scale to the correlation between the two signals.

The instantaneous angle of phase, $\theta_{x-y}(a, \tau)$, can be expressed as:

$$\theta_{x-y}(a, \tau) = tg^{-1} \frac{QuadW_{xy}(a, \tau)}{CoW_{xy}(a, \tau)} \quad (7)$$

This formulation may be used to analyse the correlation between the fluctuations at a given frequency present in two simultaneously-acquired signals. When $\theta_{x-y} = 0 \pm k360 \text{ deg}$ the analyzed signals are perfectly in phase, whereas $\theta_{x-y} = 180 \pm k360 \text{ deg}$ indicates perfect phase opposition.

3 Results and discussion

The Wavelet analysis is performed on the pressure (P_f), fluid temperature (T_f) and wall temperature (T_w) signals. The analysis is performed on a frequency range from 0.01 to 4 Hz. For the processing of the signals, an in-house-developed wavelet tool has been used (see e.g. [13], [19]), by imposing the following parameters show in table 3, where number of samples is $N_{WT} = 2^n = f_{ac} t_{an}$.

Table 2. Wavelet parameters.

a		401	
ω_0		2π	
f_{min} [Hz]		0.01	
f_{max} [Hz]		4	
	Pressure	Temperature	g-level
f_{ac} [Hz]	200	50	5
n	12	10	7
N_{wt}	4096	1024	128
t_{an} [s]	20.48	20.48	25.6

The Wavelet analysis is conducted through the following steps:

- a) choice of the relevant time range (Microgravity period);
- b) definition of the dominant frequency;
- c) analysis of gravity acceleration as a possible disturbance;
- d) comparison of the Wavelet Scalogram and the Power Spectrum of the fluid pressure, fluid temperature and wall temperature signals;
- e) determination of the Wavelet Scalogram and the Power Spectrum of the fluid pressure signal at each heat input level;
- f) identification of the dominant frequency of the fluid pressure signal for each heat input level;
- g) comparison between the fluid pressure signal recorded at the evaporator and the signal recorded at the condenser through wavelet cross scalogram, wavelet local correlation coefficient and instantaneous angle of phase;
- h) identification of the mean instantaneous angle of phase at the dominant frequency between the fluid pressure signal recorded at the evaporator and at the condenser for each heat load input;
- i) identification of the mean time lag and then the mean velocity at the dominant frequency between the fluid pressure signal recorded at the evaporator and the signal recorded at the condenser for each heat load input.

3.1 The microgravity period

As thoroughly explained in [17], since the tube diameter is larger than the capillary limit on ground, this kind of Pulsating Heat Pipe has been actually proved to operate as a series of Loop Thermosyphons when gravity is present, while it switches to the Pulsating Heat Pipe mode (oscillating slug flow) when the gravity field is absent, i.e. during the microgravity period of a parabolic flight. In this framework, the time frequency analysis of the fluid pressure signal gives a further proof of such a change in the operating mode. Figure 2a shows the temporal trend of the gravity field during a parabolic manoeuvre consisting of three periods: the first hyper-gravity (20 s) during the aircraft ascent, the microgravity period at the top of the parabola (20s) and the second hyper-gravity period (20s) during the aircraft recovery. Figure 2b shows the temporal trend of the fluid pressure signal close to the evaporator zone synchronized with the gravity trend, where the red lines highlight the microgravity period. The sudden change in the fluid pressure fluctuation is clearly visible in terms of amplitude during the microgravity period but it is only the wavelet processing of the fluid pressure signal that reveals, by means of the scalogram (fig. 3c), the existence of energy peaks, apparently at a given frequency only during the microgravity period. For these reasons the WT analysis have been performed for all the heat input levels only during the microgravity duration.

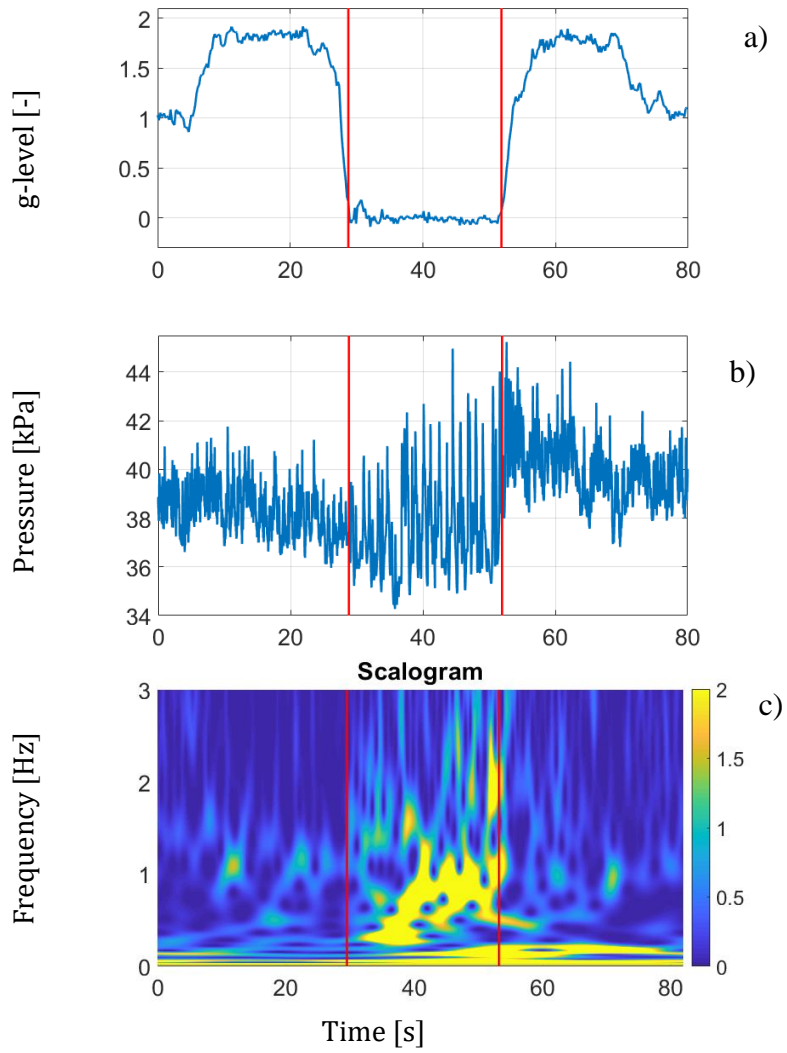


Figure 2: a) g-level and b) fluid pressure temporal trend during a typical flight parabola; Wavelet analysis results, c) scalogram and d) power spectrum.

3.2 Definition of dominant frequency

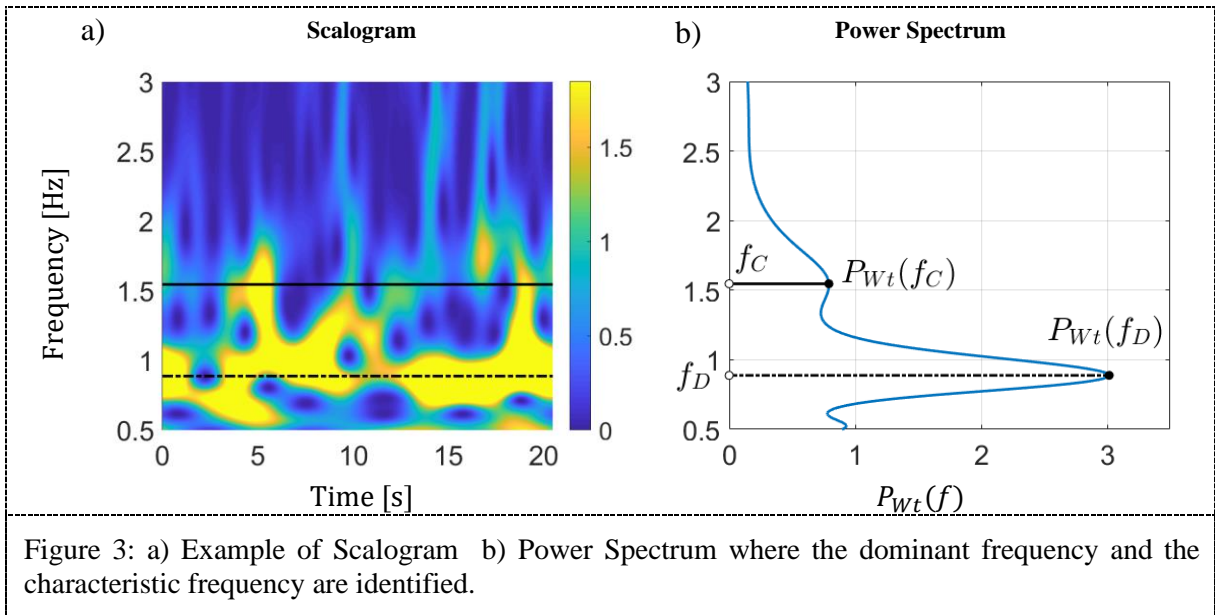
Given the wavelet power spectrum $P_{Wt}(f)$, in the domain $\text{Dom}(P_{Wt})$, the dominant frequency (f_D) shall be defined as the frequency at which the absolute maximum of the function is $P_{Wt}(f)$ occur. Thus, from an analytical point of view:

$$\forall f \in \text{Dom}(P_{Wt}) \quad P_{Wt}(f) < P_{Wt}(f_D) \quad (8)$$

Since the wavelet power spectrum $P_{Wt}(f)$ may present more than one peak, relative-maximum frequencies, also called characteristic frequencies, are also defined. The relative-maximum frequencies f_C exist if $\exists \text{SubDom}(P_{Wt})$ with $f_D \notin \text{SubDom}(P_{Wt})$ such that:

$$\forall f \in \text{SubDom}(P_{Wt}) \quad P_{Wt}(f) \leq P_{Wt}(f_C) \quad (9)$$

The dominant frequency (f_D) will be indicated in the Scalogram and in the Power Spectrum graphs as a black dashed line instead the characteristic, or secondary, frequency (f_C) as a black solid line (Figure 4b). Once defined the dominant and the characteristic frequencies from the wavelet spectrum, it is possible to evaluate also their temporal continuity from the scalogram. Notice that such a rigorous procedure allows to compare the results of different authors according to a unique analytical definition.



3.3 Noise

The gravitational acceleration g signal is analysed too by means of the WT method to ensure that the aircraft g -gitter does not add spurious frequencies to the pressure or temperature signals. In this case, the acquisition frequency is $f_{ac}^g = 50$ Hz, $N_{Wt}^g = 128$ is chosen for the analysis time $t_{an}^g = 25,6$ s, and with the g -level range $-0,1 \leq g \leq 0,1$ (Figure 5a). In the Wavelet Scalogram and in the Power Spectrum, there are not dominant or characteristic frequencies, as

show in Figure 5 (b-c). Although the magnitude of the energy contribution of the g signal is almost negligible, the frequency limit $f \geq 0.5 \text{ Hz}$ (red hatch) ensures a noise-free analysis.

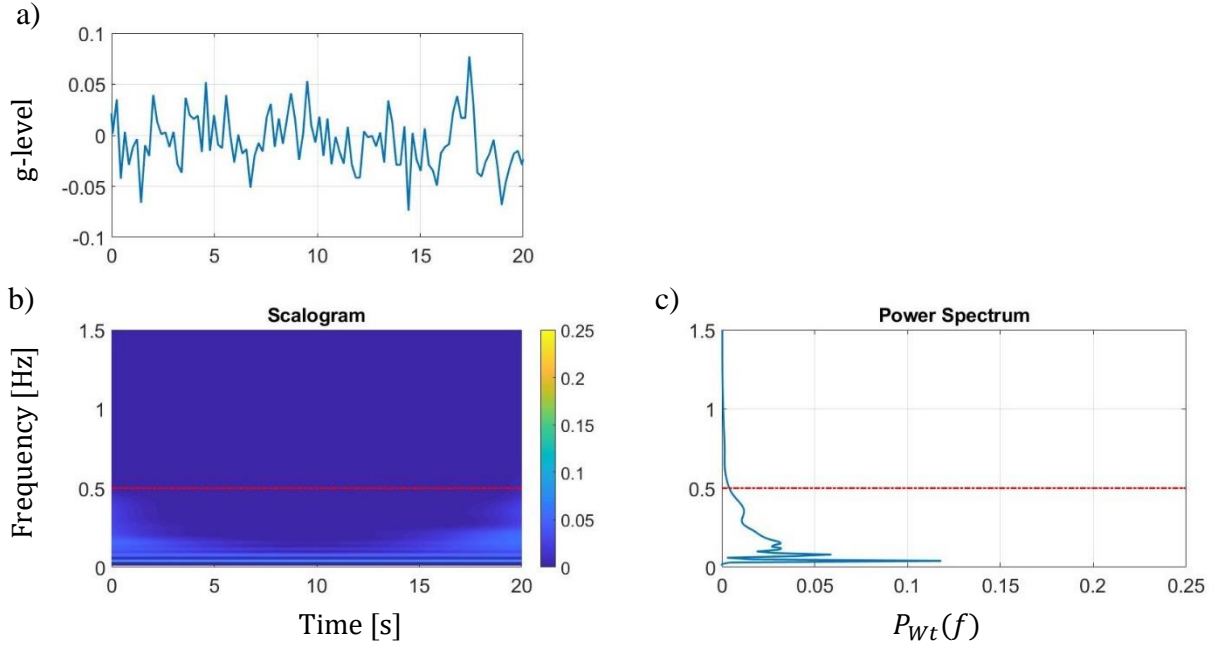
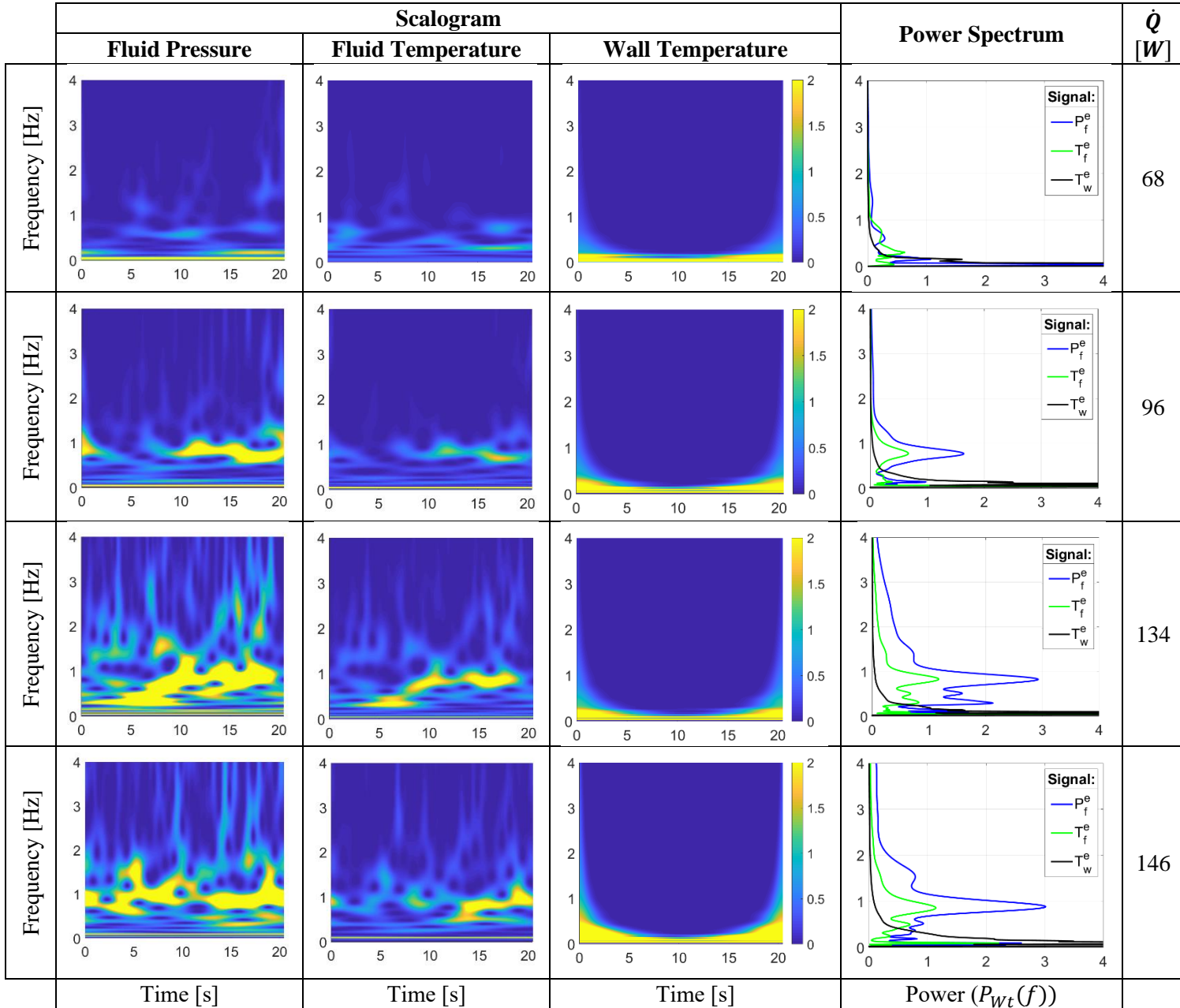


Figure 4: a) g-level temporal trend from the accelerometer; b) Wavelet Scalogram and c) Power Spectrum.

3.4 Signal choice

This section compares the results of WT analyses obtained using different signals, fluid pressure (P_f^e), fluid temperature (T_f^e) and wall temperature (T_w^e) signals recorded in the evaporator zone during the same time interval. For the pressure signal, the acquisition frequency is $f_{Ac}^P = 200 \text{ Hz}$ and $N_{Wt}^P = 4096$ is chosen for an analysis time $t_{An}^P = 20,48 \text{ s}$. Instead, for the temperature signal, the acquisition frequency is $f_{Ac}^T = 50 \text{ Hz}$ and $N_{Wt}^T = 1024$ is chosen for an analysis time $t_{An}^T = 20,48 \text{ s}$. The Scalograms for each signal are shown in Figure 5 and the Power Spectrum of all three signals in a unique plot (P_f^e , T_f^e , T_w^e respectively blue, green, black line). The fluid temperature signal appears to have the same dominant frequency as the pressure signal, with a lower energy content. The wall temperature signal, instead, does not show appreciable results in any frequency range, also according to Monroe at al. [11], and this is due to the thermal impedance of the tube wall: the PHP envelope and its thermal inertia act as a low-pass filter RC circuit on the signal. For these reasons, this work considers only the pressure signal at the evaporator P_f^e and condenser P_f^c .



2 **Figure 5:** Wavelet Scalogram and Power Spectrum of the fluid pressure signal (P_f^e blue line), the fluid
3 temperature (T_f^e green line) and the wall temperature (T_w^e black line), for each heat load input.

4 **3.5 Pressure signal wavelet analysis**

5 The Wavelet Scalogram and Power Spectrum of a signal for each heat load level are represented
6 in Figure 7, respectively. The dominant frequency is identified by the black dashed line and by
7 the value as shown in Section 3.2. The dominant frequency falls in the range 0,6 - 0,9 Hz. Since
8 each heat input level has been tested at least four times to guarantee repeatability, the all the
9 results are analysed, compared and summarized and in Figure 8 resuming the dominant
10 frequency (y-axis) occurring at each power input (x-axis). A linear interpolation of all the data

11 (dashed line in figure 8) shows that the value of the dominant frequency increases with
 12 increasing heat load input.

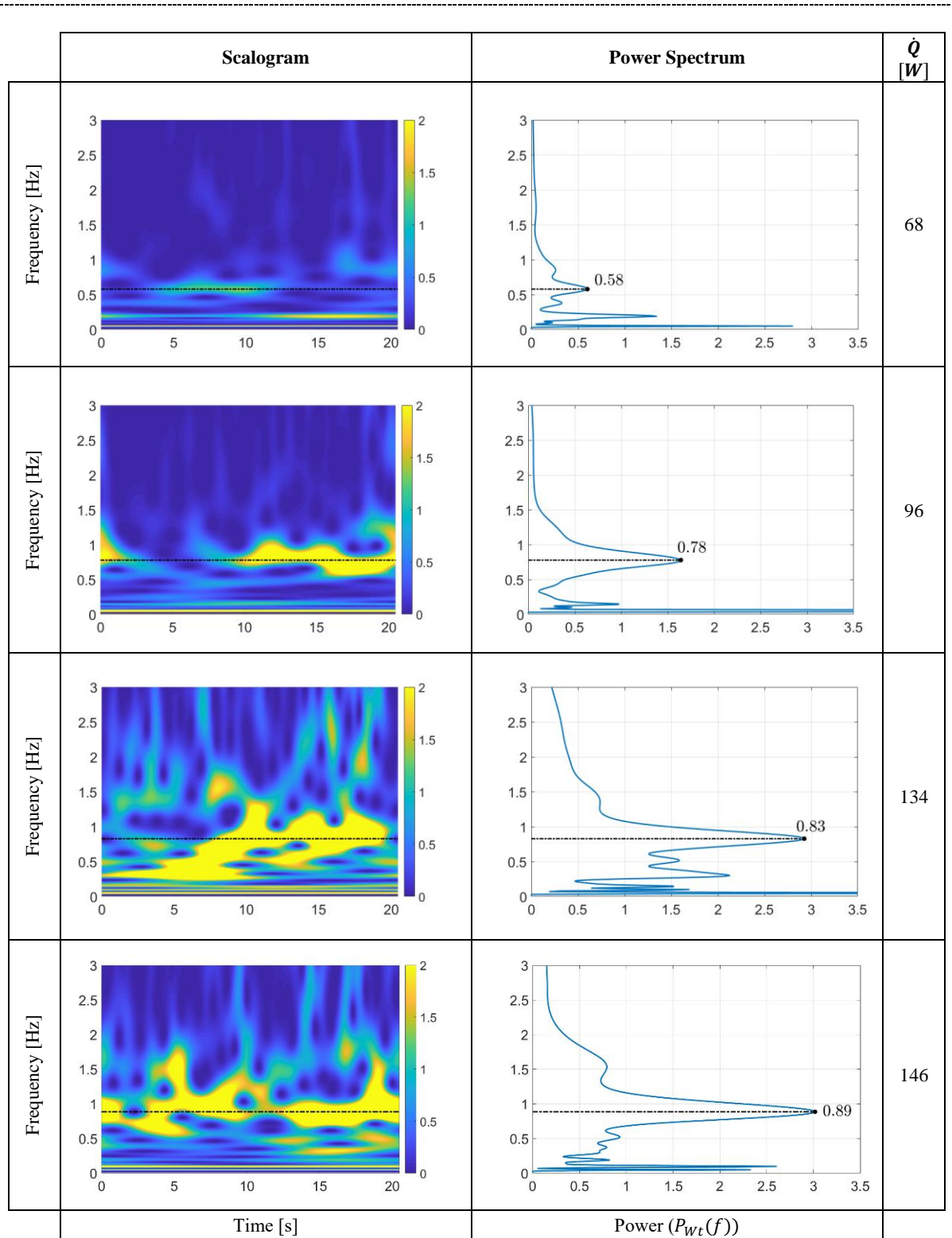


Figure 6: Wavelet Scalogram and Power Spectra of the fluid pressure signal (P_f^e) at each heat load input

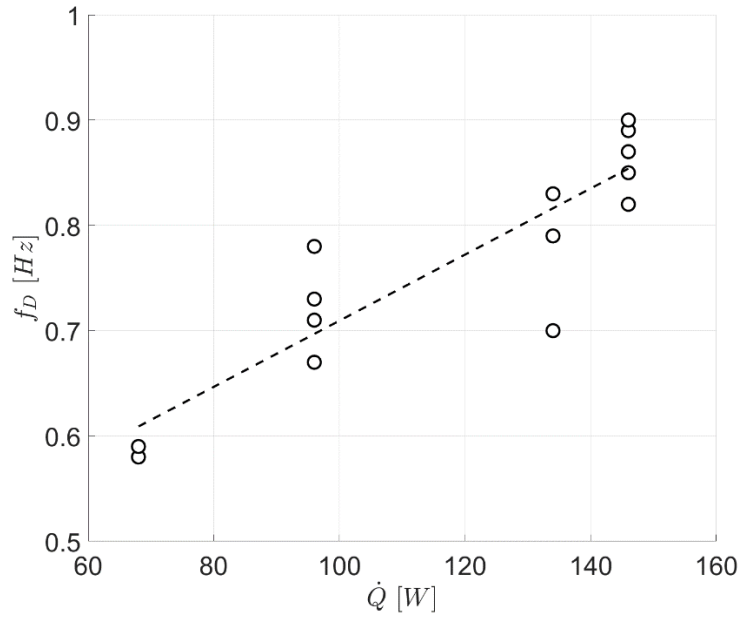


Figure 7: Dominant frequency trend with increasing heat load input of the fluid pressure signal.

13 3.6 Cross correlation and fluid mean velocity

14 As shown in Section 2.3, the co-scalogram of the cross-wavelet transform identifies the
 15 frequencies where energy peaks are present both for the evaporator (P_f^e) and the condenser (P_f^c)
 16 (Figure 9 a). Their contribution to the correlation is derived from the Instantaneous Angle of
 17 Phase, θ_{e-c} (Figure 9 b). As often happens, since trends are not clearly detectable, θ_{e-c} plots
 18 have been filtered by using the cross scalogram as mask (Figure 9 c).

19
 20
 21
 22
 23
 24
 25
 26
 27
 28
 29

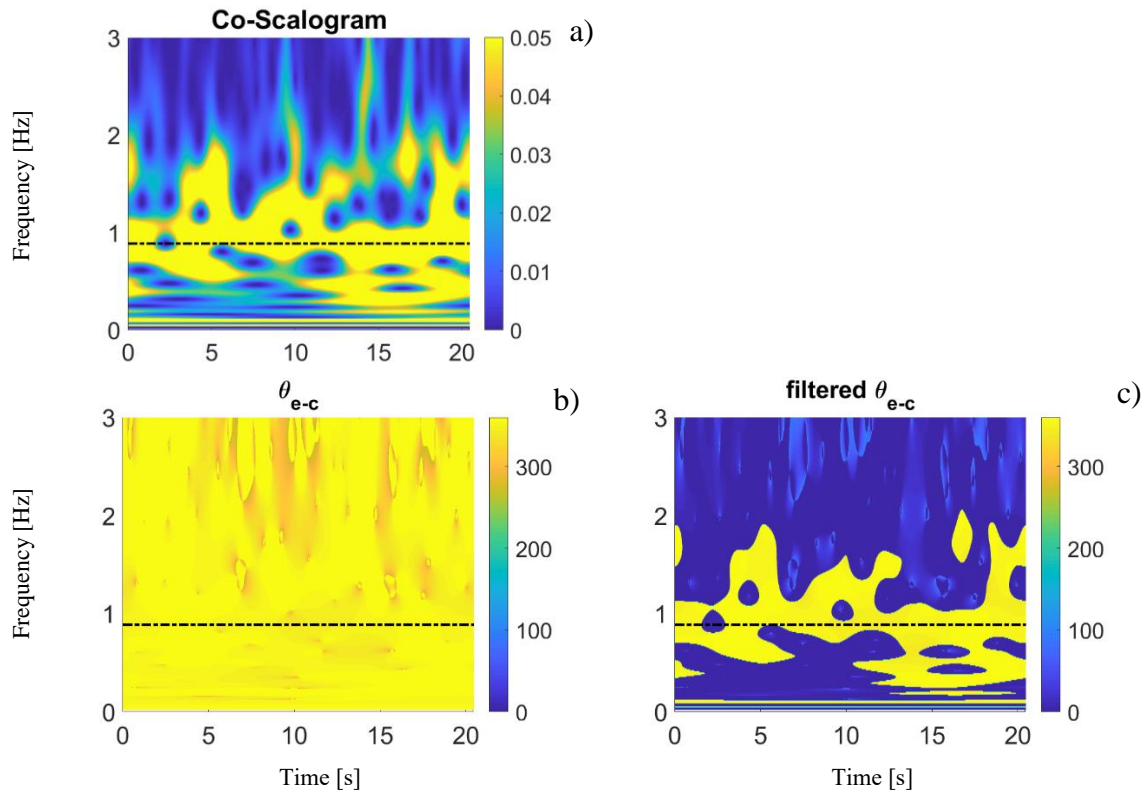


Figure 8: comparison between the fluid pressure signal at the evaporator (P_f^e) and the fluid pressure signal at the condenser (P_f^c). Wavelet Cross Scalogram (a). Instantaneous angle of phase θ_{e-c} (b) and related filtered (c).

30 Later, these filtered plots are integrated over time, obtaining the mean filtered $\bar{\theta}_{e-c}|_{f_D}$ plot as
 31 shown in the second column of Figure 10 second column. The plots in the third column display
 32 the residual points percentage (r.p. [%]), i.e. the fraction of meaningful data after the filtering
 33 procedure. The r.p. percentage obtained at 68 W is below the 50%, meaning that data are not
 34 reliable after the filtering procedure. All the other power levels show r.p. percentages above
 35 70%, meaning that the most of data fall close to the dominant frequency. The mean filtered
 36 $\bar{\theta}_{e-c}|_{f_D}$ is between 350 deg and 355 deg at high heat load inputs and 311 deg at low heat load
 37 input.

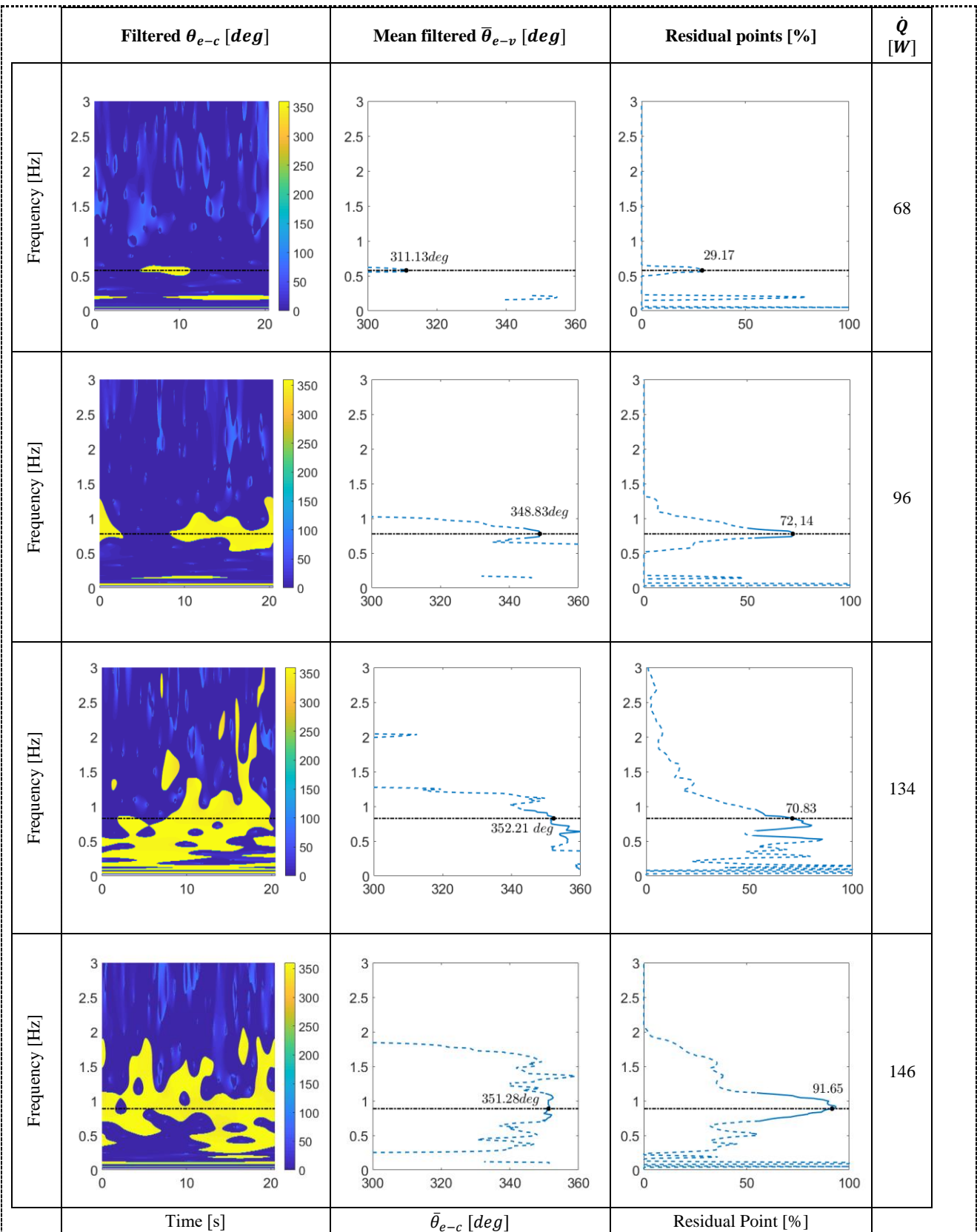


Figure 9: Filtered instantaneous angle of phase θ_{e-c} , mean filtered instantaneous angle of phase $\bar{\theta}_{e-c}$ and residual point for each heat load input.

Moreover, assuming the two signals have the same dominating frequency f , the time lag between two signals can be evaluated. In particular, the mean time lag $\bar{t}_{e-c}|_f$ between the two signals $P^e(t)$ and $P^c(t)$ at a given frequency f is:

$$\bar{t}_{e-c}|_{f_D} = \frac{\bar{\theta}_{e-c}|_{f_D}}{360f_D} \quad (10)$$

where $\bar{\theta}_{e-c}|_f(a)$ is the mean angle over time at the given frequency f (one value for each given a). Values of $\bar{t}_{e-c}|_{f_D}$ fall in the range 1.5 – 1.1 s. Assuming a Eulerian frame, the mean phase shift between the two pressure signals can be interpreted as the mean time needed by a batch of fluid to travel from the evaporator to the condenser. So, in first approximation, the mean time shift between the two pressure signals can be related to the fluid mean velocity of the fluid batch moving between the evaporator and the condenser as follows:

$$\bar{v}_{e-c}|_{f_D} = \frac{L}{\bar{t}_{e-c}|_{f_D}} \quad (11)$$

where $L = L_{PHP} = 0.14 \text{ m}$ is the distance between the evaporator and condenser measurement points as shown in figure 1.

Table 4. Resume of the wavelet analysis results.

DAY	p	\dot{Q} [W]	f_D [Hz]	$r.p. _{f_D}$ [%]	$\bar{\theta}_{e-c} _{f_D}$ [deg]	$\bar{t}_{e-c} _{f_D}$ [s]	$\bar{v}_{e-c} _{f_D} = \bar{v}_{WT}$ [m/s]	\bar{v}_{IR} [m/s]
I	8	68	0,58	29,17	311,13	1,49	0,09	0.08
I	24	68	0,59	25,88	338,91	1,60	0,09	0.06
I	11	96	0,78	72,14	348,83	1,25	0,11	0.12
I	12	96	0,73	57,64	355,49	1,36	0,10	0.08
I	14	96	0,71	80,52	353,55	1,39	0,10	-
I	15	96	0,67	47,46	344,90	1,43	0,10	0.08
I	16	134	0,70	77,39	357,06	1,42	0,10	-
I	17	134	0,83	70,83	352,21	1,18	0,12	0,11
I	18	134	0,83	69,02	352,31	1,18	0,12	-
I	19	134	0,79	80,47	342,48	1,21	0,12	-
II	11	146	0,85	93,92	353,96	1,16	0,12	-
II	12	146	0,89	91,65	351,28	1,10	0,13	0,13
II	13	146	0,82	72,46	352,38	1,20	0,12	0.11
II	14	146	0,87	80,66	356,00	1,14	0,12	0.11
II	15	146	0,90	81,23	354,87	1,10	0,13	-

The mean velocity $\bar{v}_{e-c}|_{f_D}$ have been calculated for each parabola and falls in the range 0,09 - 0,13 m/s. All the data collected are summarized in the Table 4. This order of magnitude is comparable with the velocity values obtained with infrared analyses described in subsection 2.2, summarized in the last column of Table 4.

The velocity values achieved from the wavelet analysis ($\bar{v}_{e-c}|_{f_D} = \bar{v}_{WT}$) and from the infrared analysis (\bar{v}_{IR}) were also compared in the v/\dot{Q} plot (Figure 11).

Figure 11 show that the value of the mean velocity increases with increasing heat load input. The repeatability of the results is indicated by the white/grey/black colors. For instance, as show in Table 4, at $\dot{Q} = 134 \text{ W}$, the results $\bar{v}_{e-c}|_{f_D} = 0,12 \text{ m/s}$ is repeated three times (black dots in Figure 11), while $\bar{v}_{e-c}|_{f_D} = 0,10 \text{ m/s}$ is repeated one time (white dot in Figure 11). The high repeatability of the results shows that the velocity is not much sensitive to frequency variations of $\Delta f = 0,04 \text{ Hz}$ ($0,83 < f_D < 0,79$), while it varies for $\Delta f = 0.13 \text{ Hz}$ ($0,83 < f_D < 0,70$), at heat load input given ($\dot{Q} = 134 \text{ W}$).

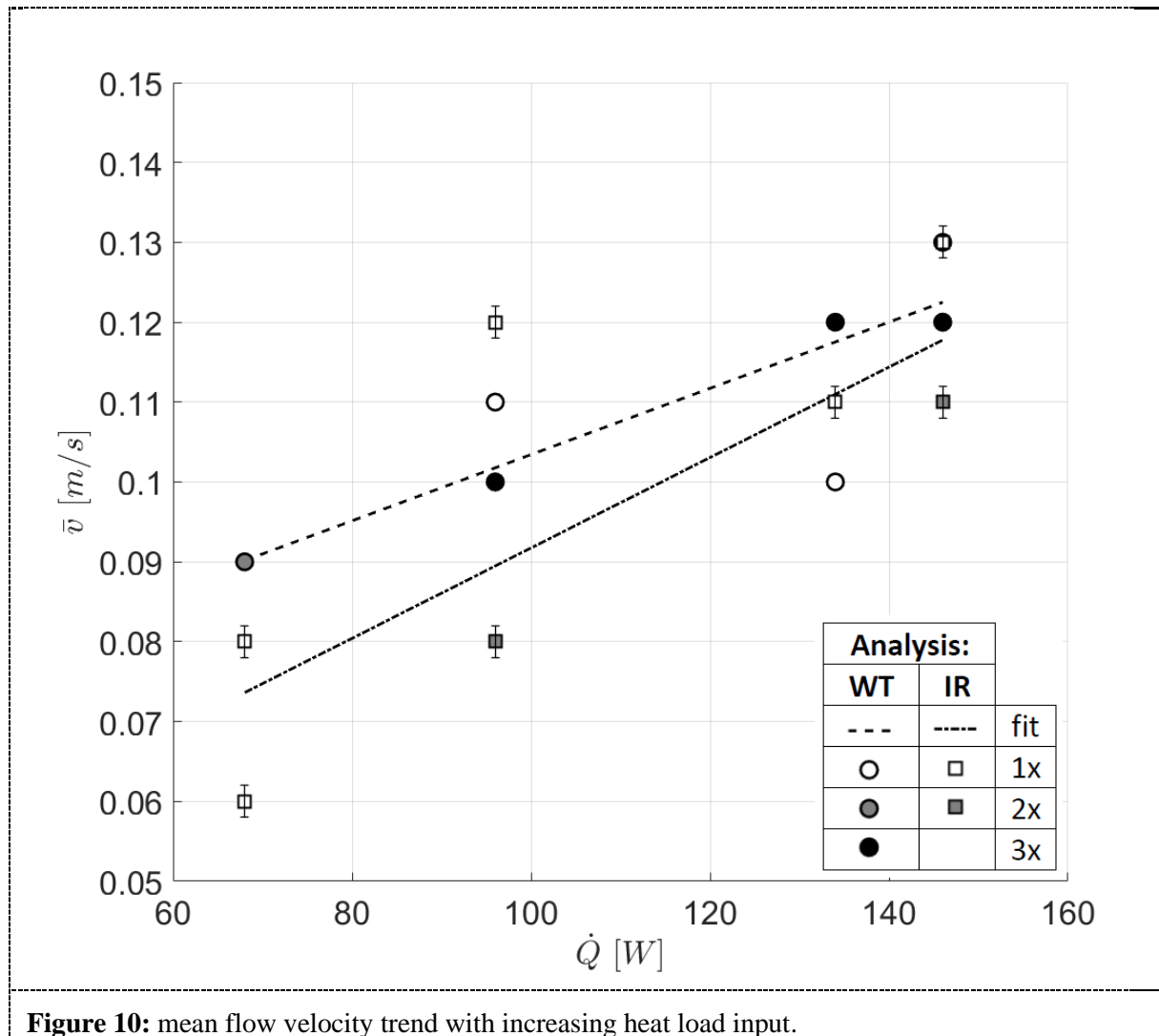


Figure 10: mean flow velocity trend with increasing heat load input.

Investigating the fluid motion by means of two pressure transducers combined with the time frequency analysis, constitute a novel and promising tool that allows to provide an order of magnitude of the fluid mean velocity without any visualization technique, thus simplifying the experimental hardware.

4 Conclusions

The fluid pressure signals at the evaporator and the condenser of a Pulsating Heat Pipe tested in microgravity conditions and with varying heat load input have been processed through a

wavelet analysis to provide a rigorous definition of dominant frequency in the fluid motion. The investigation also allowed to relate the dominant frequencies to the heat input levels and, finally to provide an esteem of the mean flow velocity through the cross correlation between the two signals. The main outcomes of the present work are:

- the wall temperature signal of the hybrid PHP cannot be used for Wavelet analysis, due to the thermal impedance of the tube wall while the pressure signal is the most suitable;
- in general, the dominant frequency should be defined as the frequency related to the absolute maximum in the Power spectrum;
- the value of the dominant frequency of the pressure signals falls in the range 0,6-0,9 Hz and increases with increasing heat load input;
- the cross correlation between the two pressure signals allow to evaluate the mean phase shift, which itself can be related to the mean oscillating flow velocity. For the present case it falls in the range 0,09 - 0,13 m/s and increases with increasing heat load input which is physically consistent;
- the velocity values obtained from the wavelet analysis and from the infrared analysis were in good agreement.

The possibility to investigate the average local fluid mean velocity only by means of pressure signals processed with a wavelet tool, constitutes an important step forward the characterization of the PHP behaviour and towards the validation of analytical and numerical PHP models.

References

- [1] Saha S.K., Celata G.P., “Instability in Flow Boiling in Microchannels”, *Springer Briefs in Applied Sciences and Technology*, 2016.
- [2] Rao M., Lefèvre F., Czujko P., Khandekar S., Bonjour J.,” Numerical and experimental investigations of thermally induced oscillating flow inside a capillary tube”, *Int. J. of The. Sci.* 115, 29e42, 2017.
- [3] J. L. Xu and X. M. Zhang, “Start-up and steady thermal oscillation of a pulsating heat pipe,” *Heat and Mass Transfer/Waerme- und Stoffuebertragung*, vol. 41, no. 8, 2005.
- [4] M. Mameli, S. Khandekar, and M. Marengo, “Are Dominant Oscillation Frequencies Always Present in Pulsating Heat Pipes?,” *Seventh International Symposium on Two-Phase Systems For Ground And Space Applications, Beijing, China, September 17-21, 2012*, 2012.
- [5] M. Mameli, M. Marengo, and S. Khandekar, “Local heat transfer measurement and thermo-fluid characterization of a pulsating heat pipe,” *International Journal of Thermal Sciences*, vol. 75, 2014.
- [6] A. Takawale, S. Abraham, A. Sielaff, P. S. Mahapatra, A. Pattamatta, and P. Stephan, “A comparative study of flow regimes and thermal performance between flat plate pulsating heat pipe and capillary tube pulsating heat pipe,” *Applied Thermal Engineering*, Feb. 2019.
- [7] J. D. Fairley, S. M. Thompson, and D. Anderson, “Time–frequency analysis of flat-plate oscillating heat pipes,” *International Journal of Thermal Sciences*, vol. 91, 2015.
- [8] K. Ishii and K. Fumoto, “Temperature visualization and investigation inside evaporator of pulsating heat pipe using temperature-sensitive paint,” *Applied Thermal Engineering*, vol. 155, Jun. 2019.

- [9] H. Peng, P. F. Pai, and H. Ma, “Nonlinear thermomechanical finite-element modeling, analysis and characterization of multi-turn oscillating heat pipes,” *International Journal of Heat and Mass Transfer*, vol. 69, 2014.
- [10] G. Spinato, N. Borhani, and J. R. Thome, “Understanding the self-sustained oscillating two-phase flow motion in a closed loop pulsating heat pipe,” *Energy*, vol. 90, Oct. 2015.
- [11] J. G. Monroe, Z. S. Aspin, J. D. Fairley, and S. M. Thompson, “Analysis and comparison of internal and external temperature measurements of a tubular oscillating heat pipe,” *Experimental Thermal and Fluid Science*, vol. 84, 2017.
- [12] G. Buresti, G. Lombardi, and J. Bellazzini, “On the analysis of fluctuating velocity signals through methods based on the wavelet and Hilbert transforms,” in *Chaos, Solitons and Fractals*, 2004, vol. 20, no. 1.
- [13] A. Mariotti, G. Buresti, G. Gaggini, and M. v. Salvetti, “Separation control and drag reduction for boat-tailed axisymmetric bodies through contoured transverse grooves,” *Journal of Fluid Mechanics*, vol. 832, 2017.
- [14] N. Zhao, H. Ma, and X. Pan, “Wavelet Analysis of Oscillating Motions in an Oscillating Heat Pipe,” 2012.
- [15] R. G. Chi, W. S. Chung, and S. H. Rhi, “Thermal characteristics of an oscillating heat pipe cooling system for electric vehicle Li-ion batteries,” *Energies*, vol. 11, no. 3, Feb. 2018.
- [16] S. Khandekar, A. P. Gautam, and P. K. Sharma, “Multiple quasi-steady states in a closed loop pulsating heat pipe,” *International Journal of Thermal Sciences*, vol. 48, no. 3, Mar. 2009.
- [17] Mamelì M., Catarsi A., Mangini D., Pietrasanta L., Michè N., Marengo M., Di Marco P., Filippeschi S., Start-up in Microgravity and Local Thermodynamic States of a Hybrid Thermosyphon/Pulsating Heat, *Applied Thermal Engineering*, Vol 158, 113771, 2019.
- [18] Catarsi, A., Fioriti, D., Mamelì, M., Filippeschi, S., Di Marco, P., Accuracy analysis of direct infrared temperature measurements of two-phase confined flows, 16th International Heat Transfer Conference, Beijing, China, 10-15 August 2018.
- [19] A. Mariotti, “Axisymmetric bodies with fixed and free separation: Base-pressure and near-wake fluctuations,” *Journal of Wind Engineering and Industrial Aerodynamics*, vol. 176, May 2018.
- [20] E.W. Lemmon, M.L. Huber, M.O. McLinden, NIST Standard Reference Database 23: Reference Fluid Thermodynamic and Transport Properties-refprop, Version 8.0, National Institute of Standards and Technology, Standard Reference Data Program, Gaithersburg, 2007.

Acknowledgments

The present work is carried forward in the framework of the ESA MAP Project INWIP (4000115115/15/NL/PG and the EPSRC UK HyHP Project (EP/P013112/1). Thanks to the NOVESPACE team in Bordeaux, and especially to Ms. Alexandra Jacquemet for their ground and flight technical support. Thanks to Davide Fioriti, Roberto Manetti, Massimo Ciampalini, Franco Peticca, Davide Della Vista for their essential technical contribution and to Dr. Daniele Mangini, Marco Bernagozzi and Matteo Pozzoni for their support and the participation to the parabolic flight campaign. Special thanks to Dr. Balazs Toth and Dr. Daniele Mangini for their constant interest and support and to Prof. Guido Buresti for his valuable suggestions. Furthermore, the team would like to thank the TRP project, and the laboratory TEC-MMG at ESA/ESTEC for lending the MWIR camera.